

# Prospects for a 95 GeV Higgs Boson at Future Higgs Factories with Transformer Networks

Yabo Dong,<sup>1,\*</sup> Manqi Ruan,<sup>2,†</sup> Kun Wang,<sup>3,‡</sup> Haijun Yang,<sup>4,§</sup> and Jingya Zhu<sup>1,¶</sup>

<sup>1</sup>*School of Physics and Electronics,*

*Henan University, Kaifeng 475004, China*

<sup>2</sup>*Institute of High Energy Physics, Chinese Academy of Sciences, Beijing 100049, China*

<sup>3</sup>*College of Science, University of Shanghai for  
Science and Technology, Shanghai 200093, China*

<sup>4</sup>*State Key Laboratory of Dark Matter Physics,  
Key Laboratory for Particle Astrophysics and Cosmology (MOE),  
Shanghai Key Laboratory for Particle Physics and Cosmology (SKLPPC),  
School of Physics and Astronomy & Tsung-Dao Lee Institute,  
Shanghai Jiao Tong University, Shanghai 200240*

(Dated: October 29, 2025)

## Abstract

Several experimental analyses have reported mild excesses near 95 GeV that could indicate the presence of a light Higgs-like scalar. We study the phenomenology of such a state within the flipped Next-to-Two-Higgs-Doublet Model (N2HDM-F) at the proposed Circular Electron–Positron Collider (CEPC). The light scalar  $S$  is investigated through the Higgsstrahlung process  $e^+e^- \rightarrow Z(\mu^+\mu^-)S$  with  $S \rightarrow \tau^+\tau^-$  and  $S \rightarrow b\bar{b}$  decay modes. A full Monte Carlo simulation including detector effects is performed to estimate the discovery reach and precision measurement potential. To maximize the sensitivity, we employ particle-level transformer networks (ParT and MiParT) that exploit correlations among all reconstructed objects. Compared with a cut-based baseline, improves the expected measurement precision by a factor of 2.4 in the  $\tau\tau$  channel and 1.4 in the  $bb$  channel. For viable benchmark points in the N2HDM-F, the attainable precisions on the signal rate reach 1.0% and 0.63%, respectively. Interpreted in a model-independent framework, the CEPC can achieve a  $5\sigma$  discovery for  $\mu_{\tau\tau}^{ZS} > 1.6 \times 10^{-2}$  and  $\mu_{bb}^{ZS} > 4.2 \times 10^{-3}$ , and reach a 1% precision for  $\mu_{\tau\tau}^{ZS} > 0.96$  and  $\mu_{bb}^{ZS} > 0.13$ . These results highlight the potential of particle-level machine learning techniques in extending the light-Higgs exploration program at future lepton colliders.

---

\* [dongyb@henu.edu.cn](mailto:dongyb@henu.edu.cn)

† [manqi.ruan@ihep.ac.cn](mailto:manqi.ruan@ihep.ac.cn)

‡ Corresponding author: [kwang@usst.edu.cn](mailto:kwang@usst.edu.cn)

§ [haijun.yang@sjtu.edu.cn](mailto:haijun.yang@sjtu.edu.cn)

¶ Corresponding author: [zhujy@henu.edu.cn](mailto:zhujy@henu.edu.cn)

## CONTENTS

I. Introduction	3
II. The broken-phase flipped N2HDM	6
A. Model Setup	6
B. Parameter Scan and Constraints	8
C. Features of the N2HDM-F Scenario	9
III. Monte Carlo Simulation	10
A. Signal and Background Modeling	10
B. Event Generation and Selection in the $\tau\tau$ Channel	13
C. Event Generation and Selection in the $bb$ Channel	16
IV. Application of ParT and MIParT Networks	18
A. Performance on the $\tau\tau$ Channel	18
B. Performance on the $bb$ Channel	22
C. Comparative Discussion	24
V. Conclusions	27
Acknowledgments	29
References	29

## I. INTRODUCTION

The discovery of the Higgs boson at the LHC in 2012 [1, 2] completed the last missing piece of the Standard Model (SM) puzzle. However, several unresolved questions continue to cast shadows over the SM, among which the origin of the baryon asymmetry of the Universe remains one of the most compelling [3–5]. According to the Sakharov conditions [6], three criteria must be fulfilled to generate the observed matter–antimatter asymmetry: (i) baryon number violation, (ii) sufficient  $C$  and  $CP$  violation, and (iii) a departure from thermal equilibrium. In the SM, the  $C$  and  $CP$  violation is too weak, and the electroweak phase transition (EWPT) associated with the 125 GeV Higgs boson is merely a smooth crossover

rather than a strong first-order transition [7, 8]. These shortcomings strongly indicate that new physics beyond the SM is required to account for the baryon asymmetry. A minimal yet well-motivated approach is to extend the Higgs sector by introducing additional scalar fields. Such extensions can naturally provide new sources of  $C$  and  $CP$  violation and can also induce a strong first-order EWPT, thereby realizing the necessary out-of-equilibrium conditions [9].

Several experimental excesses near 95 GeV have been reported across different search channels, suggesting intriguing hints of a light scalar resonance. The earliest indication dates back to 2003, when the LEP experiment observed a local significance of  $2.3\sigma$  in the process  $e^+e^- \rightarrow ZS (\rightarrow b\bar{b})$  around 98 GeV, where  $S$  denotes a hypothetical lighter Higgs boson [10]. In 2018, the CMS Collaboration reported a local excess of  $2.8\sigma$  in the  $gg \rightarrow S \rightarrow \gamma\gamma$  channel at a mass of 95.3 GeV, based on the combined 8 TeV ( $19.7 \text{ fb}^{-1}$ ) and 13 TeV ( $35.9 \text{ fb}^{-1}$ ) datasets [11]. Further hints appeared in 2022, when CMS reported a  $3.1\sigma$  excess in the  $pp \rightarrow S \rightarrow \tau^+\tau^-$  channel near 100 GeV [12]. More recently, in 2024, both major LHC collaborations released updated diphoton results: CMS observed a  $2.9\sigma$  excess at 95.4 GeV [13], while ATLAS reported a milder  $1.7\sigma$  excess at 95.3 GeV in  $pp \rightarrow S \rightarrow \gamma\gamma$  [14]. Taken together, these observations may point toward the existence of a light Higgs-like scalar with a mass around 95.5 GeV.

The collider phenomenology of a hypothetical 95 GeV light Higgs boson has been extensively explored in recent studies through Monte Carlo (MC) simulations [15–19]. Hadron colliders, such as the Large Hadron Collider (LHC), operate at high center-of-mass energies, enabling the exploration of a wide range of physical processes [20, 21]. However, the complex QCD background at hadron colliders poses a major challenge for precision measurements and for probing subtle new-physics signals. Our previous analysis indicates that achieving a  $5\sigma$  discovery significance in the top-pair-associated diphoton channel,  $pp \rightarrow t\bar{t}S (\rightarrow \gamma\gamma)$ , at the High-Luminosity LHC (HL-LHC) requires a production cross section exceeding approximately  $0.3 \text{ fb}$ . Signals with smaller cross sections may instead be probed through alternative decay channels or at future collider facilities.

Future Higgs factories, such as the Future Circular Collider (FCC-ee) [22, 23], the International Linear Collider (ILC) [24–26], and the Circular Electron-Positron Collider (CEPC) [27–30], provide a promising avenue for probing a possible 95 GeV light Higgs boson and measuring its couplings with high precision. This enhanced sensitivity stems from

the much cleaner environment of lepton colliders compared to hadron colliders. Our study focuses on the CEPC, motivated by its suitable center-of-mass energy and high integrated luminosity. The scenarios of the other two colliders will be discussed at the end of the paper. CEPC aims to study the properties of the 125 GeV Higgs boson with unprecedented accuracy and is expected to deliver over  $20 \text{ ab}^{-1}$  at 240 GeV [27–30]. Given that the dominant production mechanism for a 95 GeV scalar at the CEPC is the Higgsstrahlung process ( $e^+e^- \rightarrow ZS$ ), this work is dedicated to its detailed investigation.

In addition, machine learning (ML) has shown its potential in jet tagging tasks [31–37] in recent years. Among these, Particle Transformer (ParT) [36] and the More-Interaction Particle Transformer (MIParT) [37], which are based on the transformer architecture [38], have demonstrated outstanding performance. The quark–gluon classification accuracy reaches 0.849 and 0.851 for ParT and MIParT, respectively, corresponding to Areas Under the Curve (AUC) of 0.9203 and 0.9215. This remarkable improvement in accuracy can be attributed to the attention mechanism, which effectively captures intricate correlations among final-state particles, thereby enabling a more expressive and comprehensive representation of jet substructures. Such particle-level ML techniques hold great promise for new-physics searches, offering the potential to significantly enhance both sensitivity and measurement precision at current and future colliders.

These experimental hints have motivated theoretical interpretations within extended Higgs sectors [39–67]. Among various theoretical frameworks proposed to interpret the 95 GeV excess, the Next-to-Two-Higgs-Doublet Model (N2HDM) provides a particularly elegant solution, offering additional scalar degrees of freedom that can simultaneously account for the observed  $bb$  and  $\tau\tau$  anomalies [67–72]. In this study, we perform a comprehensive scan of the N2HDM parameter space to examine the model’s compatibility with the observed 95 GeV excess. Subsequently, a full Monte Carlo (MC) simulation and a cut-based jet-level analysis are carried out for the Higgsstrahlung process,  $e^+e^- \rightarrow ZS$ , in various final states at the 240 GeV CEPC. To further enhance the search sensitivity and measurement precision for the 95 GeV light Higgs boson, we extract features from all final-state particles and employ them to train the ParT and MIParT networks. Finally, we present a detailed discussion of the achievable parameter coverage and measurement precision at the CEPC—with and without the inclusion of machine learning—and demonstrate the model-independent discovery potential of the CEPC.

The remainder of this paper is organized as follows. In Sec. II, we briefly introduce the N2HDM and present the results of the parameter-space scan. Section III describes the full Monte Carlo simulation and the cut-based analysis strategy. The implementation of the ParT and MIParT networks, together with the corresponding performance studies and discussions, is detailed in Sec. IV. Finally, our conclusions are summarized in Sec. V.

## II. THE BROKEN-PHASE FLIPPED N2HDM

The Next-to-Two-Higgs-Doublet Model (N2HDM) extends the Standard Model by introducing an additional Higgs doublet together with a real scalar singlet field [73–75]. After electroweak symmetry breaking (EWSB), the physical scalar spectrum comprises three neutral CP-even Higgs bosons. Among them, one must correspond to the observed SM-like Higgs at 125 GeV, while another can serve as a viable candidate to explain the experimental excesses around 95 GeV.

### A. Model Setup

The Standard Model (SM) contains only one  $SU(2)_L$  Higgs doublet,  $\Phi_1$ . The next-to-two-Higgs-doublet model (N2HDM) extends the SM by introducing an additional Higgs doublet  $\Phi_2$  and a real scalar singlet field  $\Phi_S$  [73, 74]. The scalar potential of the N2HDM is given by:

$$\begin{aligned} V = & m_{11}^2 |\Phi_1|^2 + m_{22}^2 |\Phi_2|^2 - m_{12}^2 (\Phi_1^\dagger \Phi_2 + h.c.) + \frac{\lambda_1}{2} (\Phi_1^\dagger \Phi_1)^2 + \frac{\lambda_2}{2} (\Phi_2^\dagger \Phi_2)^2 \\ & + \lambda_3 (\Phi_1^\dagger \Phi_1) (\Phi_2^\dagger \Phi_2) + \lambda_4 (\Phi_1^\dagger \Phi_2) (\Phi_2^\dagger \Phi_1) + \frac{\lambda_5}{2} [(\Phi_1^\dagger \Phi_2)^2 + h.c.] \\ & + \frac{1}{2} m_S^2 \Phi_S^2 + \frac{\lambda_6}{8} \Phi_S^4 + \frac{\lambda_7}{2} (\Phi_1^\dagger \Phi_1) \Phi_S^2 + \frac{\lambda_8}{2} (\Phi_2^\dagger \Phi_2) \Phi_S^2. \end{aligned} \quad (1)$$

After electroweak symmetry breaking, the N2HDM particle spectrum contains three CP-even neutral scalars  $H_{1,2,3}$  (The masses of the three  $H_{1,2,3}$  increase in sequence), one pseudoscalar  $A$ , and a pair of charged scalars  $H^\pm$ . The electroweak sector is in the broken phase when both doublets and the singlet acquire nonzero vacuum expectation values (VEVs). In this scenario, the three CP-even scalar fields mix through a  $3 \times 3$  rotation matrix, which is given

by Ref. [75]. Then the parameters can be parameterized in terms of the mixing angles:

$$\begin{aligned} m_{H_1}, m_{H_2}, m_{H_3}, m_{H_A}, m_{H^\pm}, \\ \alpha_1, \alpha_2, \alpha_3, m_{12}^2, v, v_S, \tan\beta, \end{aligned} \quad (2)$$

where  $m_{H_1}$ ,  $m_{H_2}$ ,  $m_{H_3}$ ,  $m_{H_A}$ , and  $m_{H^\pm}$  are the mass of  $H_1$ ,  $H_1 H_2$ ,  $A$ , and  $H^\pm$ ,  $\alpha_1$ ,  $\alpha_2$ , and  $\alpha_3$  are the mixing angles of three CP-even neutral scalars,  $m_{12}^2$  is the soft  $Z_2$ -breaking parameter,  $v = 246$  GeV is the VEV of electroweak,  $v_S$  is the VEV of singlet, and  $\tan\beta$  is the VEVs ratio of two doublets.

The most interesting part of the coupling is Higgs  $H_i$  to the massive gauge bosons, the quarks, and the leptons. The reduced coupling of Higgs  $H_i$  to the massive gauge bosons  $V = W, Z$  ( $C_{H_i VV}$ ) can be given by

$$C_{H_i VV} = \begin{cases} c_{\alpha_2} c_{\beta - \alpha_1}, & i = 1, \\ -c_{\beta - \alpha_1} s_{\alpha_2} s_{\alpha_3} + c_{\alpha_3} s_{\beta - \alpha_1}, & i = 2, \\ -c_{\beta - \alpha_1} s_{\alpha_2} c_{\alpha_3} - s_{\alpha_3} s_{\beta - \alpha_1}, & i = 3, \end{cases} \quad (3)$$

where  $c_x$  indicate  $\cos(x)$  and  $s_x$  indicate  $\sin(x)$  for the angles  $x = \alpha_1, \alpha_2, \alpha_3$ , and  $\beta - \alpha_1$ .

In the flipped N2HDM (N2HDM-F) scenario, the reduced coupling of Higgs  $H_i$  to the up-type quark and lepton  $f$  ( $C_{H_i ff}$ ) can be given by

$$C_{H_i ff} = \begin{cases} s_{\alpha_1} c_{\alpha_2} / s_\beta, & i = 1, \\ (c_{\alpha_1} c_{\alpha_3} - s_{\alpha_1} s_{\alpha_2} s_{\alpha_3}) / s_\beta, & i = 2, \\ -(c_{\alpha_1} s_{\alpha_3} + s_{\alpha_1} s_{\alpha_3} c_{\alpha_2}) / s_\beta, & i = 3, \end{cases} \quad (4)$$

The reduced coupling of Higgs  $H_i$  to the down-type quark  $q_d$  ( $C_{H_i q_d q_d}$ ) can be given by

$$C_{H_i q_d q_d} = \begin{cases} c_{\alpha_1} c_{\alpha_2} / c_\beta, & i = 1, \\ -(c_{\alpha_1} s_{\alpha_2} s_{\alpha_3} + c_{\alpha_3} s_{\alpha_1}) / c_\beta, & i = 2, \\ -(c_{\alpha_1} s_{\alpha_2} c_{\alpha_3} - s_{\alpha_1} s_{\alpha_3}) / c_\beta, & i = 3, \end{cases} \quad (5)$$

In this scenario, the couplings of  $H_i$  to  $b$  quarks and to  $\tau$  leptons exhibit distinct dependences on the model parameters, which can naturally account for the observed excesses in the  $bb$  and  $\tau\tau$  channels. These coupling patterns illustrate how the flipped N2HDM (N2HDM-F) permits independent control of quark and lepton Yukawa couplings, thereby providing the flexibility required to simultaneously accommodate both anomalies.

One of the three CP-even neutral scalars must be SM-like with a mass of 125.09 GeV. If it is assumed that  $H_1$  is the candidate to explain the possible experimental excesses and that  $H_2$  is SM-like. Under this assumption, one can reparametrize the parameters in terms of effective couplings and mixing matrix elements:

$$\begin{aligned} m_{H_1}, m_{H_2}, m_{H_3}, m_{H_A}, m_{H^\pm}, m_{12}^2, v_s \\ C_{H_2 VV}^2, C_{H_2 t\bar{t}}^2, \text{sign}(R_{23}), R_{13}, \tan\beta, \end{aligned} \quad (6)$$

where  $C_{H_2 VV}^2$  and  $C_{H_2 t\bar{t}}^2$  are the effective couplings of  $H_2$  to massive gauge bosons and top-quark,  $R_{13,23}$  are the mixing matrix elements between  $H_{1,2}$  and the singlet field.

## B. Parameter Scan and Constraints

We performed a random scan over the parameter space of the N2HDM-F using the package `ScannerS_v2.0.0` [76, 77]. With the mass of  $m_{H_2}$  fixed at 125.09 GeV, the remaining 11 parameters were varied within the following ranges:

$$\begin{aligned} 95 < m_{H_1} < 96 \text{ GeV}, & \quad \text{sign}(R_{23}) = \pm 1, \\ 300 < m_{H_3, A} < 1500 \text{ GeV}, & \quad 580 < m_{H^\pm} < 1500 \text{ GeV}, \\ 0.8 < \tan\beta < 10, & \quad -1 < R_{13} < 1, \\ 0.7 < C_{H_2 VV}^2 < 1.0, & \quad 0.7 < C_{H_2 t\bar{t}}^2 < 1.2, \\ 10^{-3} < m_{12}^2 < 5 \times 10^5 \text{ GeV}^2, & \quad 1 < v_s < 3000 \text{ GeV}. \end{aligned} \quad (7)$$

The following constraints are considered:

- Constraints from perturbative unitarity: The constraint require the eigenvalues  $\mathcal{M}_{2 \rightarrow 2}^i$  of the  $2 \rightarrow 2$  scattering matrix  $\mathcal{M}_{2 \rightarrow 2}$  satisfy

$$|\mathcal{M}_{2 \rightarrow 2}^i| < 8\pi \quad (8)$$

at tree level [78].

- Constraints from vacuum stability: The package of `EVADE` [79, 80] is used to test the stability at tree-level.
- Constraints from B physics and electroweak precision observables: The global fit result of Ref. [81] on oblique parameters and flavour constraints at  $2\sigma$  level are used.

- Constraints from Higgs Searches and SM-like Higgs Measurements: For the additional scalars direct search constraints, the effective coupling approximation is exact to interface to the `HiggsBounds-5.10.0` package [82] at the 95% confidence level using. For the SM-like Higgs Measurements, `HiggsSignal-2.6.0` package [83] use 109 degrees of freedom data to calculate the  $\chi$  of this model and. The SM  $\chi^2$  is 85.8 and

$$\Delta\chi^2 = \chi^2_{\text{N2HDM-F}} - \chi^2_{\text{SM}} < 6.18 \quad (9)$$

is required.

### C. Features of the N2HDM-F Scenario

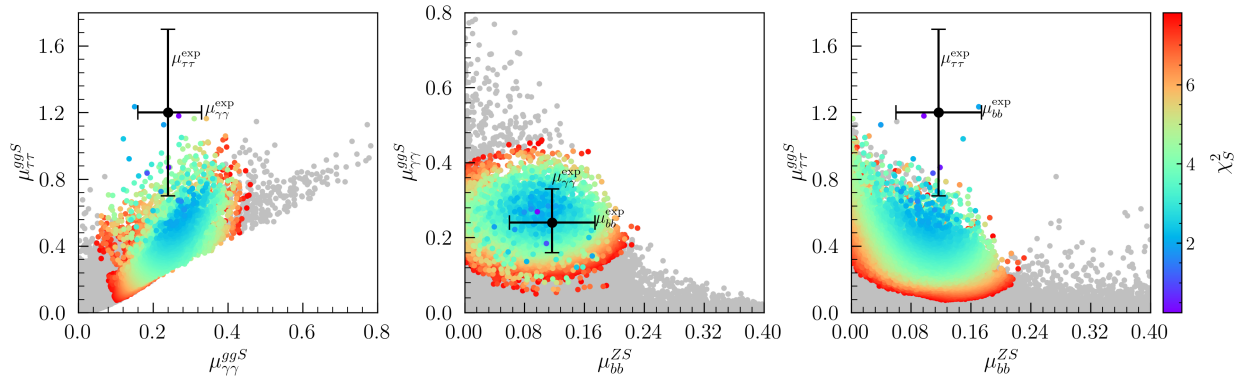


FIG. 1. surviving samples under the above constraints in the  $\mu_{\tau\tau}^{ggS}$  versus  $\mu_{\gamma\gamma}^{ggS}$  plane (left panel), the  $\mu_{\gamma\gamma}^{ggS}$  versus  $\mu_{bb}^{ZS}$  plane (middle panel), and  $\mu_{\tau\tau}^{ggS}$  versus  $\mu_{bb}^{ZS}$  plane (right panel) with colors indicating the fit result of  $\chi_S^2$  and the gray samples having  $\chi_S^2 > 7.82$ .

Fig. 1 shows the surviving samples under the above constraints in the  $\mu_{\tau\tau}^{ggS}$  versus  $\mu_{\gamma\gamma}^{ggS}$  plane (left panel), the  $\mu_{\gamma\gamma}^{ggS}$  versus  $\mu_{bb}^{ZS}$  plane (middle panel), and  $\mu_{\tau\tau}^{ggS}$  versus  $\mu_{bb}^{ZS}$  plane (right panel), respectively. The colors indicate the fit result of  $\chi_S^2$ , which is defined as

$$\chi_S^2 = \frac{(\mu_{\tau\tau}^{ggS} - \mu_{\tau\tau}^{\text{exp}})^2}{(\Delta\mu_{\tau\tau}^{\text{exp}})^2} + \frac{(\mu_{\gamma\gamma}^{ggS} - \mu_{\gamma\gamma}^{\text{exp}})^2}{(\Delta\mu_{\gamma\gamma}^{\text{exp}})^2} + \frac{(\mu_{bb}^{ZS} - \mu_{bb}^{\text{exp}})^2}{(\Delta\mu_{bb}^{\text{exp}})^2}, \quad (10)$$

where  $\mu_{xx}^{\text{exp}}$  and  $\Delta\mu_{xx}^{\text{exp}}$  are central values of three experimental excesses and relevant errors in  $\tau\tau$ ,  $bb$ , and  $\gamma\gamma$  at  $1\sigma$  level. They can be parameterized as  $\mu_{\tau\tau}^{\text{exp}} = 1.2_{-0.5}^{+0.5}$  [12],  $\mu_{bb}^{\text{exp}} = 0.117 \pm 0.057$  [10], and  $\mu_{\gamma\gamma}^{\text{exp}} = 0.24_{-0.08}^{+0.09}$  [13, 84], respectively, which marked in the Fig. 1.

The  $\mu_{xx}^{ggS}$  and  $\mu_{xx}^{ZS}$  are the signal strength in the gluon fusion channel ( $gg \rightarrow S \rightarrow xx$ ) and Higgsstrahlung channel ( $ee \rightarrow ZS(\rightarrow xx)$ ) and can be parameterized as

$$\mu_{xx}^{ggS} = \frac{\sigma(gg \rightarrow S) \times \text{Br}(S \rightarrow xx)}{\sigma_{\text{SM}}(gg \rightarrow h_{95}) \times \text{Br}_{\text{SM}}(h_{95} \rightarrow xx)} \quad (11)$$

and

$$\mu_{xx}^{ZS} = \frac{\sigma(gg \rightarrow S) \times \text{Br}(S \rightarrow xx)}{\sigma_{\text{SM}}(gg \rightarrow h_{95}) \times \text{Br}_{\text{SM}}(h_{95} \rightarrow xx)}, \quad (12)$$

where  $\sigma$  and  $\text{Br}$  denote the production cross section and branching ratio in the Beyond the Standard Model (BSM) scenario, respectively, while  $\sigma_{\text{SM}}$  and  $\text{Br}_{\text{SM}}$  represent the corresponding SM values. All three excesses can be elegantly explained within the broken phase N2HDM-F scenario. The best-fit point has a minimum  $\chi_S^2$  value of 0.24.

The branching ratios of the light Higgs boson  $S$  to  $bb$ ,  $cc$ ,  $\gamma\gamma$ ,  $\tau\tau$ , and  $gg$  in the N2HDM-F as a function of  $\alpha_1$ , for the benchmark points with  $\cos\alpha_2 = \sqrt{2}/2$  and  $\tan\beta = 2$  are shown in Fig. 2. These branching ratios are computed using the package **N2HDECY** [85]. It can be seen that  $S$  decays predominantly to  $bb$  over most of the  $\alpha_1$  range, except near  $\alpha_1 \approx \pm\pi/2$  (where  $\cos\alpha_1 \approx 0$ ). In this region, the dominant decay channels become  $\tau\tau$ ,  $cc$ , and  $gg$ . However, the  $cc$  and  $gg$  channels are associated with a larger SM background from  $Z$  boson hadronic decays [86]. Considering the channels where experimental signal excesses have been observed, we focus on the  $bb$  and  $\tau\tau$  channels in the subsequent analysis. The combination of these two channels ensures good coverage across the entire  $\alpha_1$  parameter space.

### III. MONTE CARLO SIMULATION

#### A. Signal and Background Modeling

We focus on the Higgsstrahlung process  $e^+e^- \rightarrow Z(\rightarrow \mu^+\mu^-)S(\rightarrow \tau^+\tau^-(b\bar{b}))$  at the CEPC with a center-of-mass energy of 240 GeV. In this signal process, the hypothetical scalar  $S$  is produced in association with a  $Z$  boson, where  $S$  subsequently decays into a pair of  $\tau$  leptons or  $b$  quarks, and the  $Z$  boson decays into a muon pair. Although the dominant decay channel of the  $Z$  boson is hadronic and invisible [86], we instead select the dimuon final state to utilize the recoil mass technique for reconstructing the mass of  $S$ . The recoil mass  $M_{\text{recoil}}$  is defined as [87]

$$M_{\text{recoil}} \equiv \sqrt{s - M_{\mu^+\mu^-}^2 - 2\sqrt{s}(E_{\mu^+} + E_{\mu^-})}, \quad (13)$$

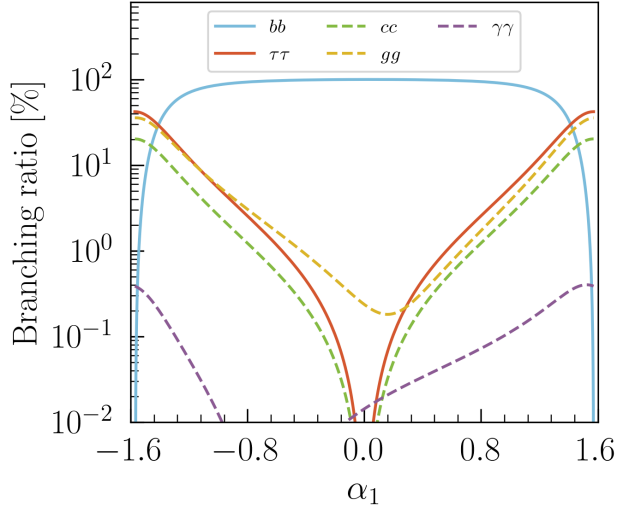


FIG. 2. The branching ratios of the light Higgs boson  $S$  to  $bb$ ,  $cc$ ,  $\gamma\gamma$ ,  $\tau\tau$ , and  $gg$  in the N2HDM-F as a function of  $\alpha_1$ , for the benchmark points with  $\cos\alpha_2 = \sqrt{2}/2$  and  $\tan\beta = 2$ .

where  $\sqrt{s}$  is the collision energy,  $M_{\mu^+\mu^-}^2$  is the square of invariant mass of dimuon, and  $E_\mu$  is the energy of muon. One can also choose  $Z$  boson decays into a pair of electrons to calculate the recoil mass, and this situation will be discussed later in the paper.

For the  $\tau\tau$  decay channel, the dominant irreducible SM background originates from the process  $e^+e^- \rightarrow \mu^+\mu^-\tau^+\tau^-$ , in which the  $\mu^+\mu^-$  and  $\tau^+\tau^-$  pairs can decay from a  $Z$  boson or a virtual photon. Additionally, the  $\tau^+\tau^-$  pair may also come from the decay of the SM Higgs boson. We also consider the reducible SM background from  $e^+e^- \rightarrow \mu^+\mu^-xx$ , where  $x$  denotes a final-state particle from a light-flavor quark, a  $b$ -quark, an electron, or a muon, which could be misidentified as a tau lepton in the detector. The leading Feynman diagrams for the signal and the irreducible backgrounds in the  $\tau\tau$  channel are shown in Fig. 3, where panel (a) corresponds to the signal, and panels (b), (c), and (d) represent the irreducible backgrounds.

In the case of the  $bb$  decay channel, the background sources are analogous to those in the  $\tau\tau$  channel, with the roles of  $bb$  and  $\tau\tau$  interchanged. Therefore, we adopt a common background process for both channels:  $e^+e^- \rightarrow \mu^+\mu^-xx$ , where  $x = u, d, c, s, b, e, \mu, \tau$ . This background comprises two components: a resonant part, in which the muon pair comes from a  $Z$  boson, and a non-resonant part, where the muon pair originates from a virtual photon.

Fig. 4 shows the surviving sample on the  $\tan\beta$  versus  $\alpha_1$  planes with the colors indicating the square of the reduced coupling of  $S$  to the  $Z$  boson  $C_{SZZ}^2$  (left panel), the cross section

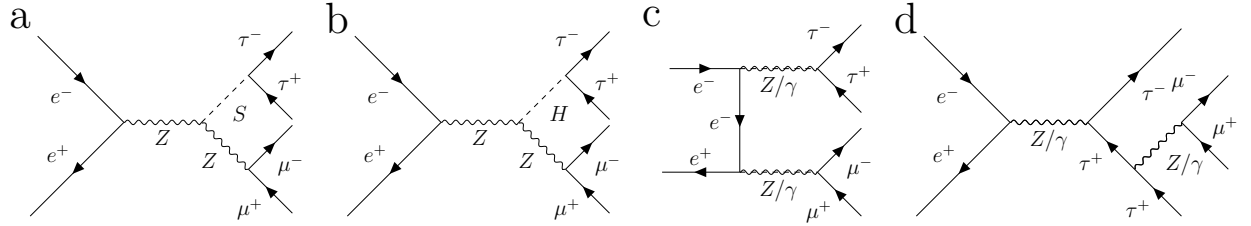


FIG. 3. The dominant Feynman diagrams of the signal and irreducible backgrounds in  $\tau\tau$  decay channel, where panel (a) corresponds to the signal, and panels (b), (c), and (d) represent the irreducible backgrounds.

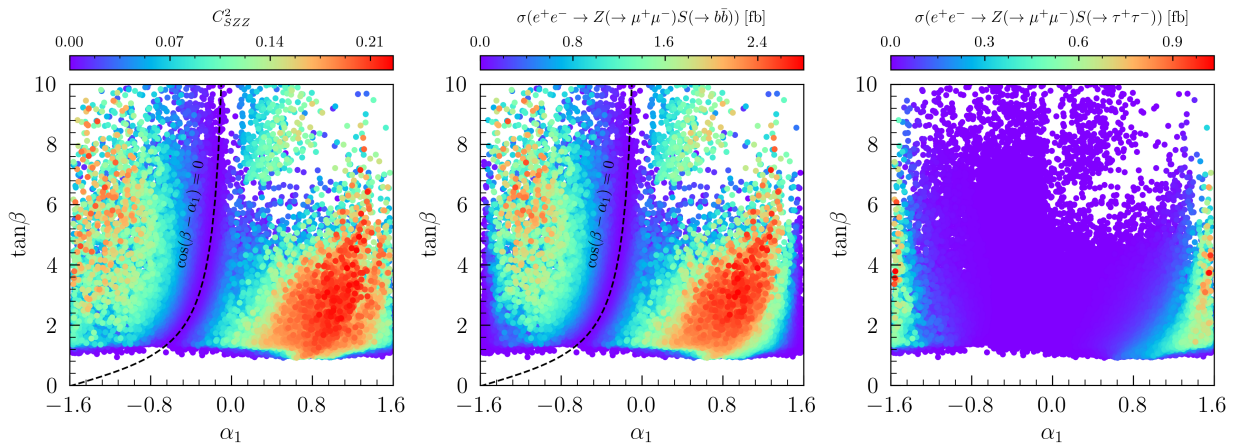


FIG. 4. Surviving sample on the  $\tan\beta$  versus  $\alpha_1$  planes with the colors indicating the square of the reduced coupling of  $S$  to  $Z$  boson (left panel), the cross section of the  $bb$  channel (middle panel), and the cross section of the  $bb$  channel (right panel).

of the  $bb$  channel (middle panel), and the cross section of the  $\tau\tau$  channel (right panel). The cross section for the  $bb$  and  $\tau\tau$  channels is computed as

$$\begin{aligned} \sigma = \sigma_{SM}(e^+e^- \rightarrow ZS)|_{m_H=95.5\text{GeV}} \\ \times C_{SZZ}^2 \cdot \text{Br}(Z \rightarrow \mu^+\mu^-) \cdot \text{Br}(S \rightarrow xx), \end{aligned} \quad (14)$$

where  $\sigma_{SM}(e^+e^- \rightarrow ZS)|_{m_H=95.5\text{GeV}}$  is the SM cross section for this process with a Higgs mass of 95.5 GeV, calculated at leading order using the **MadGraph5\_aMC@NLO\_v3.6.2** package [88, 89]. The branching ratio of  $\text{Br}(Z \rightarrow \mu^+\mu^-)$  takes the SM value of 3.3662% as given by the PDG [86]. The  $C_{SZZ}^2$  and  $\text{Br}(S \rightarrow xx)$  provided by the N2HDM-F. As shown in the left panel, the squared reduced coupling  $C_{SZZ}^2$  reaches up to 0.22 for the samples

near  $\alpha_1 \approx 0.8$ . In contrast,  $C_{SZZ}^2$  approaches zero for samples with  $\cos(\beta - \alpha_1) \approx 0$ , where the light Higg  $S$  couples weakly to massive gauge bosons and could escape detection at the CEPC. The middle and right panels indicate that the cross section for the  $bb$  channel can reach 2.8 fb for the samples with  $\alpha_1 \approx 0.8$ , while that for the  $\tau\tau$  channel reaches 1.03 fb near  $\alpha_1 \approx \pm\pi/2$ . As anticipated, except for the samples near  $\cos(\beta - \alpha_1) \approx 0$ , where the cross section of the  $bb$  channel is suppressed, the cross section of the  $\tau\tau$  channel becomes comparatively larger, as can be inferred from a combined interpretation of all three panels. In the following MC simulations, the cross sections for the  $\tau\tau$  and  $bb$  decay channels are assumed to be 1/5 of their SM values as a benchmark point.

## B. Event Generation and Selection in the $\tau\tau$ Channel

The `MadGraph5_aMC@NLO_v3.6.2` package [88, 89] is used to perform the MC simulation. During the simulation, jet clustering is performed using the `ee- $k_T$`  algorithm through `FastJet` [90], and the tau jet tagging efficiency adopted the lower limit 80% as given in Ref. [91]. The particle decays are handled by `PYTHIA_v8.2` [92] through the `MG5a-MC_PY8_interface`. The CEPC detector effects are simulated by the CEPC 4th-card with `Delphes_v3.5.0` [93, 94]. More than one million events of signal and background are generated through the Monte Carlo simulation.

In the event selection, we need two muons in the final state to calculate the recoil mass  $M_{\text{recoil}}$  to reconstruct the mass of  $S$ . Then we make the following **Basic Cut** to the event:

$$\begin{aligned} N(\mu) &\geq 2, & |\eta(\mu)| &< 2.5, \\ \Delta R(\mu_1, \mu_2) &> 0.4, & p_T(\mu) &> 10 \text{ GeV}, \end{aligned} \tag{15}$$

where  $\eta$ ,  $\phi$ , and  $p_T$  denote the pseudorapidity, azimuthal angle, and transverse momentum, respectively, and  $\Delta R = \sqrt{(\Delta\eta)^2 + (\Delta\phi)^2}$  measures the angular separation between the two muons.

In the signal process, the muon pair originates from the  $Z$  boson decay, and its invariant mass distribution is expected to peak near the  $Z$  boson mass. In contrast, a significant fraction of the background events involve muon pairs not produced from a  $Z$  boson resonance, and thus do not exhibit such a peak in their invariant mass distribution. To suppress this non-resonant background component, we apply the following  **$M_{\mu\mu}$  Cut** on the dimuon

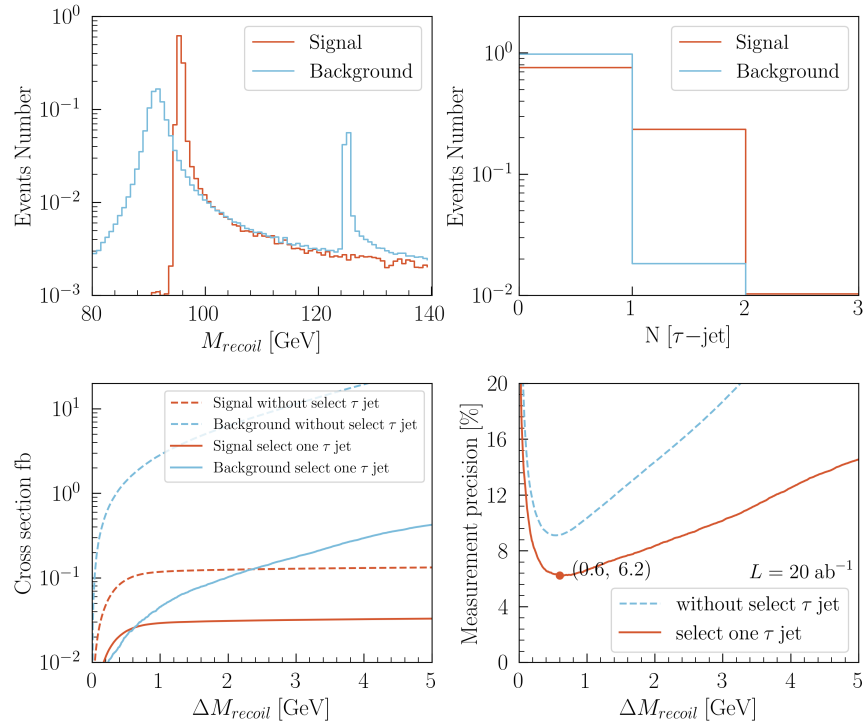


FIG. 5. The normalized event distributions of  $M_{recoil}$  (upper left panel) and  $N$  [ $\tau$ -jet] (upper right panel) for signal and background, the cross sections of the signal and background under different selections on  $M_{recoil}$  and  $N$  [ $\tau$ -jet] (lower left panel) and the corresponding measurement precision of  $\tau\tau$  channel after applying these selections (lower right panel).

invariant mass  $M_{\mu\mu}$ :

$$M_{\mu\mu} > 50 \text{ GeV}. \quad (16)$$

The normalized event distributions of  $M_{recoil}$  and the number of  $\tau$ -jet ( $N$  [ $\tau$ -jet]) for signal and background are shown in the upper left and upper right panels of Fig. 5, respectively. The upper left panel shows that the signal  $M_{recoil}$  distribution peaks sharply around 95.5 GeV, consistent with the mass of the light Higgs  $S$ . In contrast, the background distribution exhibits peaks near 91 GeV and 125 GeV corresponding to the masses of the  $Z$  boson and the SM-like Higgs boson, respectively, with the peak at 91 GeV being considerably broader. The upper right panel indicates that only about 1% of background events contain at least one  $\tau$ -jet, whereas for the signal, this fraction reaches approximately 20%. Therefore, applying selections on  $M_{recoil}$  and the number of  $\tau$ -jets can effectively suppress the background. The cross sections of the signal and background under different selections on  $\Delta M_{recoil}$  and  $N$

$[\tau\text{-jet}]$  are presented in the lower left panel are presented in the lower left panel of Fig. 5, and the corresponding measurement precision of the  $\tau\tau$  channel after selection is shown in the lower right panel. The events with  $|M_{recoil} - 95.5| \leq \Delta M_{recoil}$  are selected and the measurement precision is calculated by

$$P = \frac{\sqrt{S + B}}{S} \quad (17)$$

where  $S$  and  $B$  are the expected numbers of signal and background events, respectively, at the CEPC with an integrated luminosity of  $20 \text{ ab}^{-1}$ .

As shown in the lower left panel of Fig. 5, the background cross section exceeds that of the signal by more than an order of magnitude if no selection is applied on the number of  $\tau$ -jets, regardless of the  $M_{recoil}$  cut. However, by selecting events with at least one  $\tau$ -jet and applying an appropriate  $M_{recoil}$  cut, the signal and background cross sections can be brought to the same order of magnitude. Furthermore, for any given  $M_{recoil}$  cut, the measurement precision is significantly improved when requiring a  $\tau$ -jet in the final state. The optimal precision of 6.2% is achieved for events containing a  $\tau$ -jet and satisfying  $\Delta M_{recoil} \leq 0.6 \text{ GeV}$ . Based on this, we apply the following  **$\tau$ -jet cut** and  **$M_{recoil}$  Cut** that require

$$N[\tau\text{-jet}] \geq 1 \quad (18)$$

and

$$\Delta M_{recoil} = 0.6 \text{ GeV}. \quad (19)$$

The cut flow for the  $\tau\tau$  decay channel of the signal and background at the 240 GeV CEPC with an integrated luminosity of  $L = 20 \text{ ab}^{-1}$  is shown in Table I. It can be seen that the  **$\tau$ -jet cut** suppresses the background by approximately two orders of magnitude while retaining about 25% of the signal. The corresponding measurement precision is improved from 32.9% to 18.7%. The  **$M_{recoil}$  Cut** further suppresses the background by more than one order of magnitude and preserves about 65% of the signal to acquire a measurement precision of 6.2%.

After applying the cut on the dimuon invariant mass  $M_{\mu\mu}$ , Fig. 6 shows the normalized distributions of the transverse momenta, pseudorapidities, and azimuthal angles of the two muons and the leading jet, as well as the angular separations  $\Delta R$  between the two muons

TABLE I. Cut flow of signal and background in the  $\tau\tau$  channel at 240 GeV CEPC with  $L = 20 \text{ ab}^{-1}$ 

Cuts	Cross section [fb]		Precision [%]
	Signal	background	
Initial	0.218	84.250	29.8
Basic	0.177	72.202	34.1
$M_{\mu\mu}$	0.165	58.617	32.9
$\tau - jet$	0.040	1.094	18.7
$M_{recoil}$	0.026	0.026	6.2

and between the leading muon and the leading jet. It can be seen that further cuts on these kinematic observables do not lead to a significant improvement in signal significance or measurement precision.

### C. Event Generation and Selection in the $bb$ Channel

The event generation in the  $bb$  channel is the same as that in the  $\tau\tau$  channel, and the  $b$  jet tagging efficiency is also set to 80%. In the event selection, the **Basic Cut** and the  $M_{\mu\mu}$  **Cut** are also same as that in  $\tau\tau$  channel. The difference is that one need the final state to contain at least one  $b$  jet to suppress the reducible background. Fig. 7 shows the cross sections of the signal and background (left panel), and the  $bb$  channel measurement precision (right panel) as a function of the cut on the  $M_{recoil}$  with a requirement for a  $b$  jet and without the requirement in the final state. Different to the  $\tau\tau$  decay channel, the cross section of signal and background can be comparable just through the selecting on  $M_{recoil}$ . If select the events with one  $b$  jet can suppress the background about one order and the signal also be suppressed, which result that the measurement precision can not get its maximum value through the selection on  $M_{recoil}$ . The measurement precision can reach 1% if one selects the event required that  $\Delta M_{recoil} = 0.6 \text{ GeV}$  in the final state and without the selection on  $b$  jet. Then the  $M_{recoil}$  **Cut** are performed that require the event be satisfied for

$$|M_{recoil} - 95.5| \leq 0.6 \quad (20)$$

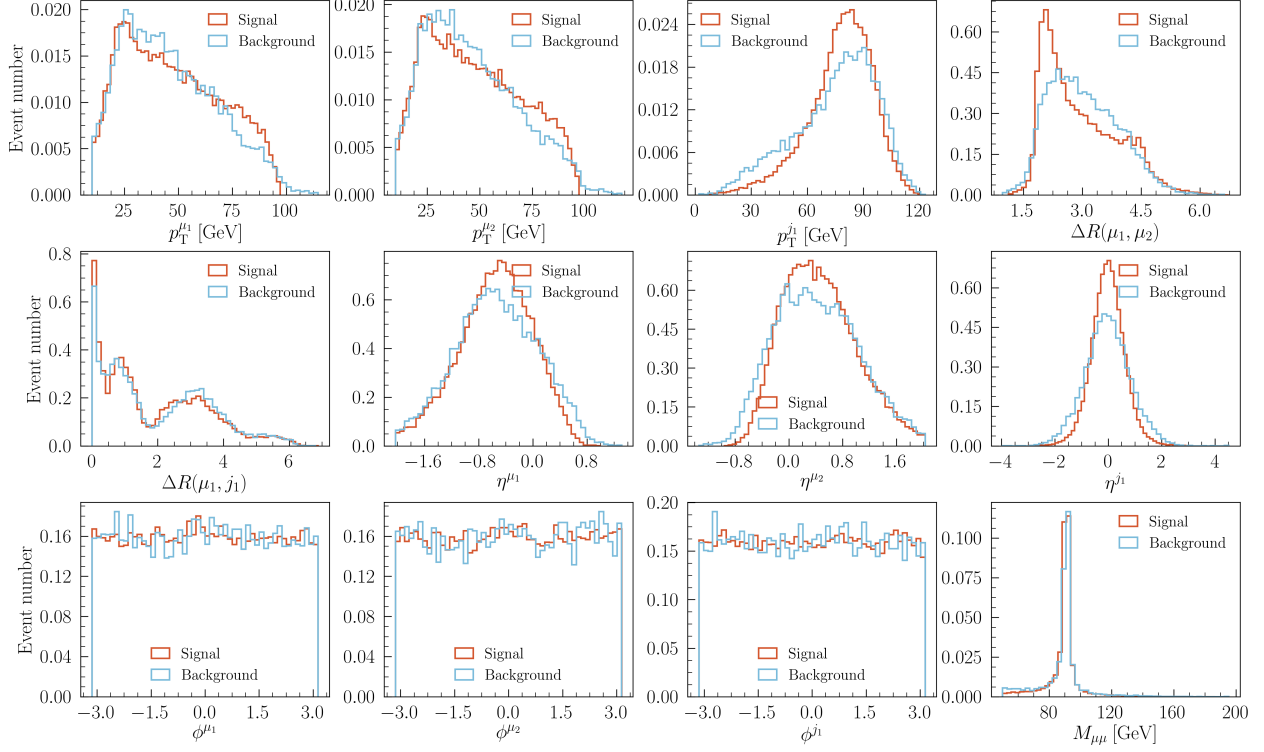


FIG. 6. The normalized distributions of the transverse momenta, pseudorapidities, and azimuthal angles of the two muons and the leading jet, as well as the angular separations  $\Delta R$  between the two muons and between the leading muon and the leading jet, after applying the cut on the invariant mass  $M_{\mu\mu}$ .

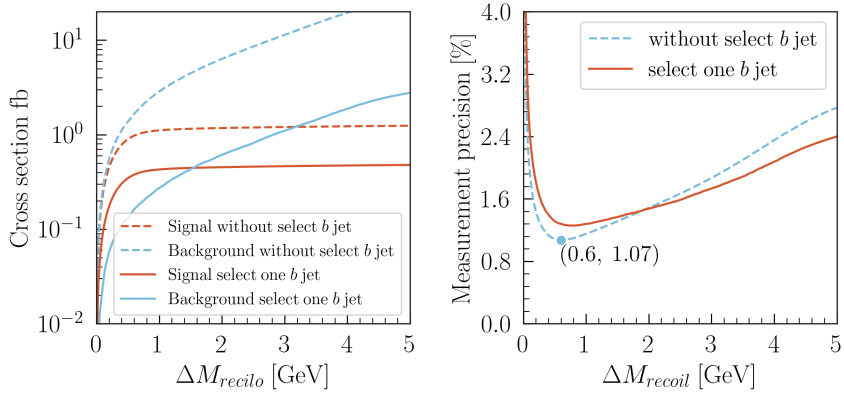


FIG. 7. The cross sections of the signal and background (left panel), and the  $bb$  channel measurement precision (right panel) as a function of the cut on the  $M_{recoil}$  with a requirement for a  $b$  jet and without the requirement in the final state.

The cut flow for the  $bb$  decay channel of the signal and background at the 240 GeV CEPC

TABLE II. Cut flow of signal and background in the  $bb$  channel at 240 GeV CEPC with  $L = 20 \text{ ab}^{-1}$ 

Cuts	Cross section [fb]		Precision [%]
	Signal	background	
Initial	2.099	84.250	3.131
Basic	1.700	72.244	3.576
$M_{\mu\mu}$	1.633	58.552	3.360
$M_{recoil}$	1.094	1.663	1.073

with an integrated luminosity of  $L = 20 \text{ ab}^{-1}$  is shown in Table II. It can be seen that the  $M_{\text{recoil}}$  Cut suppresses the background more than one order of magnitude while retaining about 67% of the signal. The corresponding measurement precision is improved from 3.4% to 1.1%. As with the  $\tau\tau$  channel, the  $bb$  channel faces a similar limitation. Even with successive cuts on jet-level kinematic observables, the measurement precision shows little improvement. The factors that restrict further improvement in the cut-based method, along with potential enhancement strategies, will be discussed in detail later in this paper.

## IV. APPLICATION OF PART AND MIPART NETWORKS

### A. Performance on the $\tau\tau$ Channel

Two main technical limitations hinder further improvement in the measurement precision of the cut-based method in the  $\tau\tau$  decay channel. First, although the  $\tau$ -tagging efficiency can reach 80%, only a small fraction of hadronically decaying  $\tau$  leptons are successfully identified as  $\tau$ -jets (approximately 25%). Second, when event selection relies on reconstructed jet information, a significant amount of information about the final-state particles is inevitably lost—some of which may be crucial. Moreover, the large number and diverse types of final-state particles make it difficult for the cut-based method to efficiently utilize all available information and extract the underlying correlations among them.

To enhance the search sensitivity for the 95 GeV light Higgs boson and improve measurement precision, we employ deep neural networks (DNNs) of Particle Transformer (ParT)

[36] and More-Interaction Particle Transformer (MIParT) [37]. ParT incorporates pairwise particle interactions into the attention mechanism, achieving superior particle tagging performance compared to standard Transformer architectures and previous machine learning models. Building upon ParT, MIParT introduces a More-Interaction Attention (MIA) mechanism that increases the dimensionality of particle interaction embeddings. This enhancement not only significantly reduces the model size but also leads to further performance gains. These models can both train directly on final-state particle-level features.

For the cut-based analysis of the  $\tau\tau$  decay channel, the available information comprises jet-level features (e.g., jet four-momenta), lepton-level observables (e.g., muon four-momenta), and event-level variables (e.g., the invariant mass and recoil mass of the dimuon system). Before training the machine learning networks, we preselect events that satisfy the **Basic Cut** of Eq.15. In the training of ParT and MIParT, the following event-level features are incorporated as inputs:

- The recoil mass of two muons:  $M_{\text{recoil}}$ .
- The invariant mass of two muons:  $M_{\mu\mu}$ .
- The average azimuthal angle of two muons:  $\phi = (\phi_{\mu_1} + \phi_{\mu_2})/2$ .
- The average pseudorapidity of two muons:  $\eta = (\eta_{\mu_1} + \eta_{\mu_2})/2$ .

The following features at the particle level are used:

- The transverse momentum of the final state particles:  $P_T^{\text{part}}$ .
- The energy of the final state particles:  $E^{\text{Part}}$ .
- The renormalized transverse momentum of the final state particles:  $R_P T^{\text{part}} = P_T^{\text{part}} / (P_T^{\mu_1} + P_T^{\mu_2})$ .
- The renormalized energy of the final state particles:  $R_E^{\text{part}} = E^{\text{part}} / (E^{\mu_1} + E^{\mu_2})$ .
- The difference between the azimuthal angle of the final state particles and the event  $\phi$ :  $\Delta\phi^{\text{part}} = \phi^{\text{part}} - \phi$ .
- The difference between the pseudorapidity angle of the final state particles and the event  $\eta$ :  $\Delta\eta^{\text{part}} = \eta^{\text{part}} - \eta$ .

- The angular separations between the final state particles to the event  $\eta$  and  $\phi$ :  

$$\Delta R^{\text{part}} = \sqrt{(\eta^{\text{part}} - \eta)^2 + (\phi^{\text{part}} - \phi)^2}.$$
- The charge of the final state particles:  $C^{\text{part}}$ .
- The kid tagging of the final state particles: Part is charged hadron, part is neutral hadron, part is photon, part is muon, or part is electron.

During data preprocessing, the following features were standardized after applying a logarithmic transformation:  $p_T^{\text{part}}$ ,  $E^{\text{part}}$ ,  $R_{p_T}^{\text{part}}$ , and  $R_E^{\text{part}}$ . To conserve computing resources, the maximum number of particles per event was set to 50. We use a total of over 300,000 signal and background events for training and evaluating the ParT and MIParT models. The dataset was split into a training set (90% of the data) and a validation set (10%). The models were trained with a batch size of 256 and an initial learning rate of 0.001. After 20 epochs, the model achieving the best performance on the validation set was selected, and its final performance was evaluated on a separate, held-out test set comprising 100,000 events. A schematic diagram comparing the jet-level cut-based analysis with our particle-level machine learning approach is presented in Fig. 8. Compared to the cut-based analysis, which only utilizes information from jets, muons, and event-level variables, our machine learning-based approach incorporates a wider set of features at the particle level. These features are difficult to leverage effectively with cut-based methods but can be fully exploited by models such as ParT and MIParT, which possess strong information processing capabilities.

Fig. 9 shows the normalized distributions of the classifier response scores for the signal and background events in the testing dataset (left panel), the background rejection rate as a function of signal efficiency (middle panel), and the  $\tau\tau$  channel measurement precision versus signal efficiency (right panel). The signal efficiency corresponds to the fraction of true signal events correctly identified, while the background rejection indicates the fraction of background events successfully rejected.<sup>1</sup> The area under the Receiver Operating Characteristic (ROC) curve (AUC) of ParT and MIParT can reach 0.9972 and 0.9979, respectively. Physically, the signal efficiency represents the fraction of true signals correctly identified,

---

<sup>1</sup> The signal efficiency is equivalent to the true positive rate (TPR),  $\varepsilon_{\text{sig}} = N_{\text{TP}}/(N_{\text{TP}} + N_{\text{FN}})$ , and the background rejection corresponds to  $1 - \text{FPR}$ , where  $\text{FPR} = N_{\text{FP}}/(N_{\text{FP}} + N_{\text{TN}})$ . Here  $N_{\text{TP}}$ ,  $N_{\text{FP}}$ ,  $N_{\text{FN}}$ , and  $N_{\text{TN}}$  denote the numbers of true positive, false positive, false negative, and true negative events, respectively.

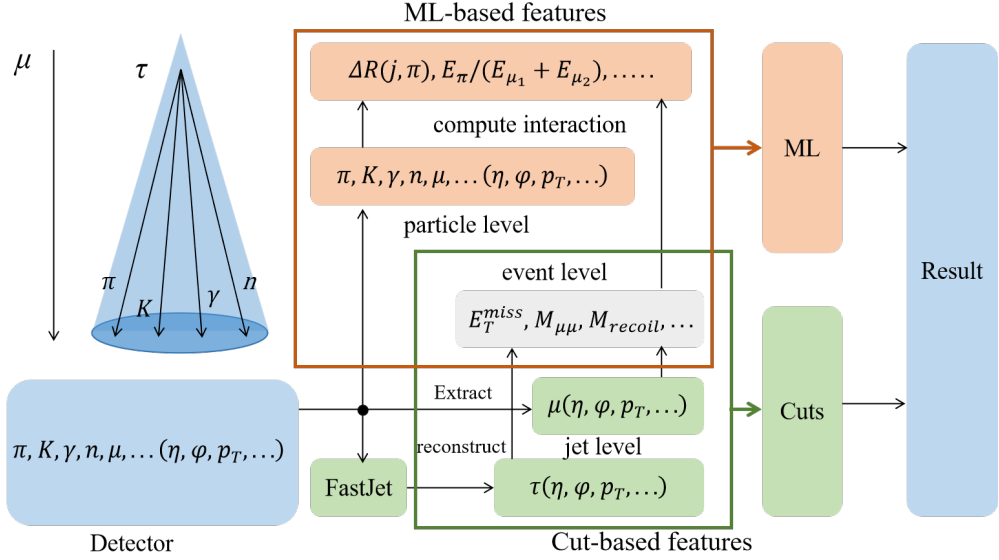


FIG. 8. The schematic diagram of the cut-based analysis at the jet level and our ML analysis at the particle level.

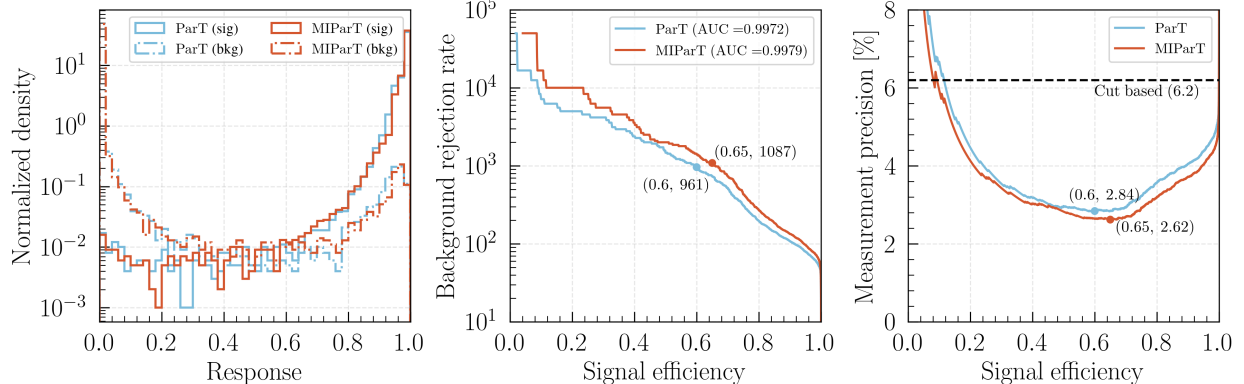


FIG. 9. The normalized distributions of the classifier response scores for the signal and background events in the testing dataset (left panel), the background rejection rate as a function of signal efficiency (middle panel), and the  $\tau\tau$  channel measurement precision versus signal efficiency (right panel) in the  $\tau\tau$  channel.

while the background rejection rate indicates the fraction of background events successfully rejected.

From the right two panels of Fig. 9, one can see that the  $\tau\tau$  channel measurement precision for ParT can reach 2.8% for the benchmark point when the signal efficiency is 0.6, with the corresponding background rejection rate is 961. In addition, the performance of MIPartT

TABLE III. The detailed data comparison without using ML and using ML in  $\tau\tau$  decay channel

method	signal efficiency	background rejection rate	precision [%]
Cut based	0.15	2777	6.2
ParT	0.60	961	2.8
MIParT	0.65	1087	2.6

is a little better. When the signal efficiency is 0.65, the measurement precision can reach 2.6%, with a corresponding background rejection rate is 1087. The MIParT exhibits superior signal efficiency and background rejection in this scenario. Relative to the 6.2% measurement precision obtained with the cut-based analysis, the precision is improved by factors of 2.2 and 2.4 when using ParT and MIParT, respectively. This improvement is consistent with the findings of Ref. [95], which demonstrated that a holistic event-level approach combined with Advanced Color Singlet Identification (ACSI) can enhance the expected precision by factors of two to six in processes where a SM-like Higgs boson is produced in association with neutrino or quark pairs and decays into light-flavor quarks or gluons. The detailed data comparison without using ML and using ML is presented in Table III. The significant improvement of the measurement precision in this ML-based analysis is manifested in the significant improvement of signal efficiency while losing a small amount of background rejection rate. It can be attributed to the efficient utilization of the features of the final state particles and the outstanding capabilities of extracting the underlying correlations among them of ParT and MIParT.

### B. Performance on the $bb$ Channel

The same ML process is also applied to the  $bb$  decay channel and the normalized distributions of the classifier response scores for the signal and background events in the testing dataset (left panel), the background rejection rate as a function of signal efficiency (middle panel), and the  $\tau\tau$  channel measurement precision versus signal efficiency (right panel) are shown in Fig. 10. The AUC of MIParT is slightly larger than that of ParT, and their AUCs can reach 0.9921 and 0.9915, respectively.

One can see that the  $bb$  channel measurement precision for ParT can reach 0.78% for

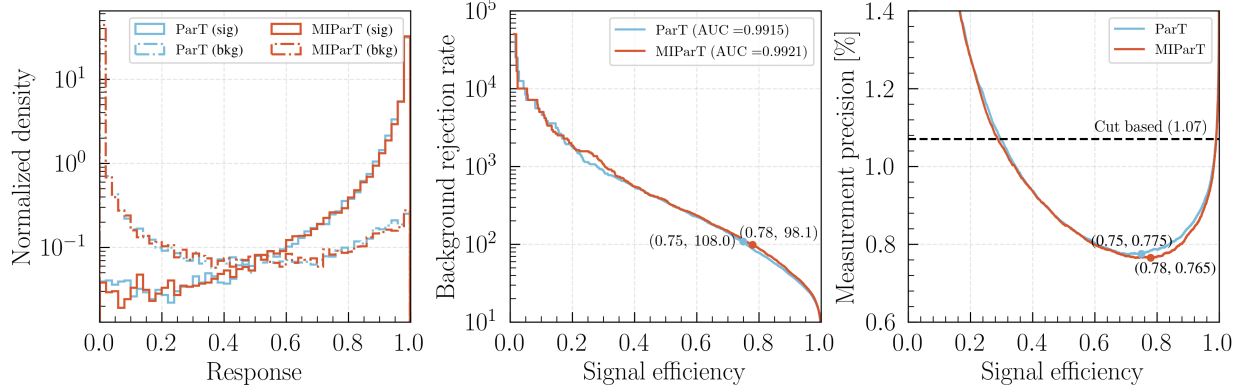


FIG. 10. The normalized distributions of the classifier response scores for the signal and background events in the testing dataset (left panel), the background rejection rate as a function of signal efficiency (middle panel), and the  $\tau\tau$  channel measurement precision versus signal efficiency (right panel) in  $\tau\tau$  channel.

the benchmark point when the signal efficiency is 0.75, with the corresponding background rejection rate is 108 from the middle and right panels of Fig. 10. As a contrast, when the signal efficiency is 0.78, the measurement precision can reach 0.77%, with a corresponding background rejection rate is 108 for ParT. Although the AUC of MIParT is slightly larger than that of ParT, there is not much difference in measurement precision in this situation. In the  $bb$  channel, the measurement precision is improved by a factor of 1.39 with our ML-based analysis, compared to the cut-based analysis precision of 1.07%. The detailed data comparison without using ML and using ML is presented in Table IV. Compared with the cut-based analysis, both signal efficiency and background rejection rate of our ML-based analysis have improved, and ultimately, measurement precision has been enhanced.

It is worth noting that the improvement achieved by MIParT over ParT is more pronounced in the  $\tau\tau$  channel than in the  $bb$  channel. This observation can be understood from the underlying event topology. The  $\tau\tau$  final state involves missing transverse energy and multiple decay modes, resulting in more diverse kinematic and substructure patterns. The additional interaction layers in MIParT enable the network to capture these complex inter-particle correlations more effectively. In contrast, the  $bb$  final state carries relatively complete and less ambiguous information; hence, the performance gain from enhanced interaction modeling in MIParT is naturally smaller.

TABLE IV. The detailed data comparison without using ML and using ML in  $bb$  decay channel

method	signal efficiency	background rejection rate	precision [%]
Cut based	0.64	43.3	1.07
ParT	0.75	108	0.78
MIParT	0.78	98.1	0.77

### C. Comparative Discussion

To assess the coverage of the N2HDM-F parameter space at the 240 GeV CEPC with and without machine learning, Fig. 11 shows the surviving samples in the  $\tan\beta$  versus  $\alpha_1$  plane. The color scale indicates the measurement precision in the  $\tau\tau$  channel without ML (upper left), with MIParT (upper right), in the  $bb$  channel without ML (lower left), and with MIParT (lower right), assuming an integrated luminosity of  $L = 20 \text{ ab}^{-1}$  at the CEPC. Gray points represent samples that can not be covered at the  $5\sigma$  signal significance level in the corresponding scenario. The signal significance is computed using the Poisson formula [96]

$$\mathcal{Z} = \sqrt{2 \left[ (S + B) \ln(1 + S/B) - S \right]}, \quad (21)$$

where  $S$  and  $B$  denote the expected numbers of signal and background events, respectively.

The following conclusions can be drawn from the Fig. 11:

- As shown in the upper two panels, samples with larger  $\tan\beta$  are more difficult to detect than those with smaller  $\tan\beta$  for the same  $\alpha_1$  in the  $\tau\tau$  channel. Meanwhile, samples with  $|\alpha|$  close to  $\pi/2$ ,  $|\sin\alpha_1|$  close to 1, are more easily detected at high precision. This observation is consistent with Eq. 4, which indicates that the coupling of  $S$  to  $\tau$  is proportional to  $\sin\alpha_1$  and inversely proportional to  $\sin\beta$ . The surviving samples with the maximum cross section in the  $\tau\tau$  channel can be detected with 2.2% precision without machine learning, and with 1.0% precision when using MIParT.
- From the lower two panels, one can see that almost all the surviving samples can be covered at the  $5\sigma$  level in the  $bb$  decay channel except the surviving samples with  $\cos(\beta - \alpha_1) \approx 0$ , as it is the dominant decay channel for most parameter space. In addition, the use of MIParT can further improve the measurement precision; the maximum can be improved from 0.86% without ML to 0.63% with MIParT.

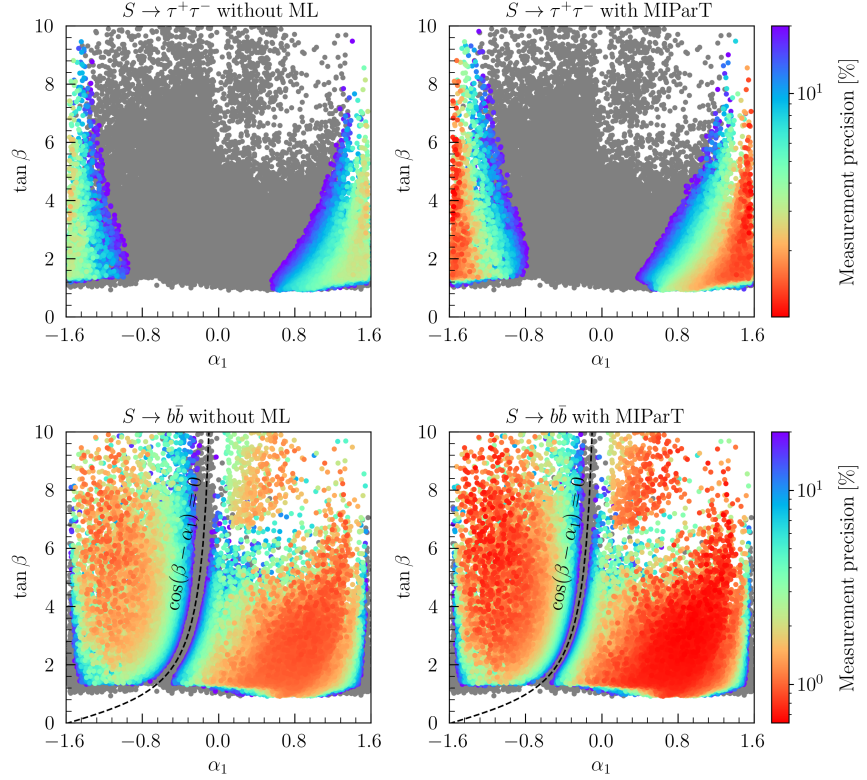


FIG. 11. The surviving samples in the  $\tan\beta$  versus  $\alpha_1$  plane. The color represents the measurement precision in the  $\tau\tau$  channel without ML (upper left), with MIParT (upper right), in the  $bb$  channel without ML (lower left), and with MIParT (lower right), based on an integrated luminosity of  $L = 20 \text{ ab}^{-1}$  at CEPC. Gray points indicate samples that cannot be covered at the  $5\sigma$  signal significance level under the corresponding scenario.

- As we expect, the samples with small  $\tan\beta$  and  $|\alpha|$  close to  $\pi/2$  are hardly be detected in  $bb$  channel, but can be detected in  $\tau\tau$  channel at high measurement precision.

For a detailed discussion on the improvement of our ML method and a quantitative analysis of the coverage capacity of the CEPC, Fig. 12 shows the measurement precision (left panel) and the cross section (right panel) as a function of the model parameter  $\alpha_1$  in  $\tau\tau$  decay channel (red lines) and  $bb$  decay channel (blue lines) for the benchmark points with  $\cos\alpha_2 = \sqrt{2}/2$  and  $\tan\beta = 2$ . Without machine learning, only samples in the range  $0.2 < \alpha_1 < 1.4$  can be measured with 1% precision in the  $bb$  decay channel, while no samples satisfy the 1% precision requirement in the  $\tau\tau$  channel. After applying MIParT, samples with  $\alpha_1 < -1.4$  or  $\alpha_1 > 1.3$  can be measured at 1% precision in the  $\tau\tau$  decay channel. Only those in the region  $-1 < \alpha_1 < 0$  remain undetectable at this precision level in both

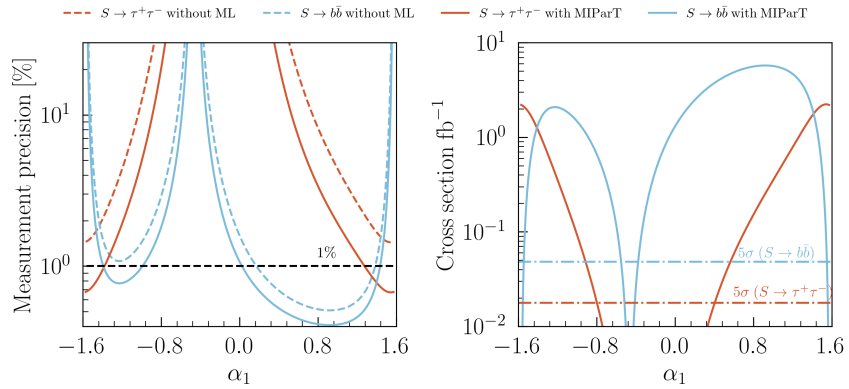


FIG. 12. The measurement precision (left panel) and the cross section (right panel) as a function of the model parameter  $\alpha_1$  in  $\tau\tau$  decay channel (red lines) and  $bb$  decay channel (blue lines) for the benchmark points with  $\cos\alpha_2 = \sqrt{2}/2$  and  $\tan\beta = 2$ .

the  $bb$  and  $\tau\tau$  channels. In terms of  $5\sigma$  discovery potential at the 240 GeV CEPC with an integrated luminosity of  $L = 20 \text{ ab}^{-1}$ , signal regions are considered covered if the cross section exceeds  $0.018 \text{ fb}$  in the  $\tau\tau$  channel or  $0.044 \text{ fb}$  in the  $bb$  channel. The only parameter region not accessible at this significance is  $-0.54 < \alpha_1 < -0.38$ .

The CEPC measurement precisions of 5%, 2%, and 1% for the  $\tau\tau$  and  $bb$  channels are presented in Fig. 13 on the  $\text{Br}(S \rightarrow \tau\tau)$  versus  $C_{SZZ}$  plane (left panel) and the  $\text{Br}(S \rightarrow b\bar{b})$  versus  $C_{SZZ}$  plane (right panel), respectively. The shadow area can be covered at  $5\sigma$  level and the regions above the contours correspond to parameter spaces accessible at the corresponding precision. The signal strength in the  $\tau\tau$  or  $bb$  decay channel from the Higgsstrahlung process is defined as

$$\mu_{\tau\tau \text{ (}bb\text{)}}^{ZS} = C_{SZZ}^2 \times \frac{\text{Br}(S \rightarrow \tau^+\tau^- \text{ (}b\bar{b}\text{)})}{\text{Br}_{\text{SM}}(h_{95} \rightarrow \tau^+\tau^- \text{ (}b\bar{b}\text{))}}. \quad (22)$$

Based on this definition, samples with  $\mu_{\tau\tau}^{ZS} > 0.0162$  and  $\mu_{bb}^{ZS} > 0.0042$  can be covered at the  $5\sigma$  level in the  $\tau\tau$  and  $bb$  channels, respectively. Furthermore, samples satisfying  $\mu_{\tau\tau}^{ZS} > 0.083$ , 0.3, or 0.96 can be measured with a precision of 5%, 2%, or 1%, respectively. Similarly, in the  $bb$  channel, precisions of 5%, 2%, and 1% are achievable for  $\mu_{bb}^{ZS} > 0.02$ , 0.056, and 0.13, respectively. These results are also applicable to other multi-Higgs models featuring a light Higgs with a mass around 95.5 GeV.

The signal channel with the  $Z$  boson decays to electrons has also been investigated and shows similar performance. When the electron and muon channels of the  $Z$  boson are

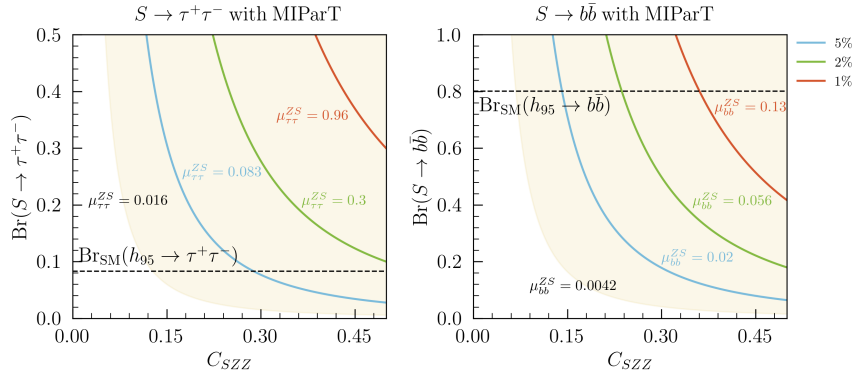


FIG. 13. The CEPC sensitivity in the  $\tau\tau$  and  $bb$  channels on the  $\text{Br}(S \rightarrow \tau\tau)$  versus  $C_{SZZ}$  plane (left panel) and  $\text{Br}(S \rightarrow bb)$  versus  $C_{SZZ}$  plane (right panel). The shadow area can be covered at  $5\sigma$  level and the range upper the lines can be detected at corresponding precision.

combined, the measurement precision is further improved by approximately 30%.

## V. CONCLUSIONS

In this work, we have explored the prospects for detecting a light Higgs-like scalar with a mass of 95 GeV at the Circular Electron–Positron Collider (CEPC), focusing on the  $\tau\tau$  and  $bb$  decay modes. Event-level and particle-level observables, together with their correlations, are used as inputs to train deep neural networks based on the Particle Transformer (ParT) and its more-interactive variant (MIParT). Compared with a conventional cut-based analysis, the machine-learning approach when applied to the same Monte Carlo samples improves the expected measurement precision by a factor of 2.4 in the  $\tau\tau$  channel and 1.4 in the  $bb$  channel. This improvement originates from the efficient exploitation of final-state particle information and the superior capability of transformer architectures to capture global event features and inter-particle dependencies.

Most of the parameter space in the flipped Next-to-Two-Higgs-Doublet Model (N2HDM-F) can be probed at the  $5\sigma$  significance level when the  $\tau\tau$  and  $bb$  channels are combined, except in regions near  $\cos(\beta - \alpha_1) \approx 0$ , where the coupling of the 95 GeV scalar  $S$  to the  $Z$  boson is highly suppressed, leading to very small production rates. For the benchmark points with the largest cross sections, a measurement precision of 2.2% (0.86%) can be achieved in the  $\tau\tau$  ( $bb$ ) channel using a cut-based analysis, which improves to 1.0% (0.63%) when the

MIParT architecture is employed.

To present the results in a model-independent way, we express the sensitivities in terms of the normalized signal strength

$$\mu_{xx}^{ZS} \equiv \frac{\sigma(e^+e^- \rightarrow ZS) \times \text{Br}(S \rightarrow xx)}{\sigma(e^+e^- \rightarrow ZH_{\text{SM}}) \times \text{Br}(H_{\text{SM}} \rightarrow xx)}$$

at  $\sqrt{s} = 240$  GeV. Based on this definition, the machine-learning-based analysis yields the following sensitivity reaches:

- **$\tau\tau$  channel:** A  $5\sigma$  discovery can be achieved for  $\mu_{\tau\tau}^{ZS} > 1.6 \times 10^{-2}$ , while a 1% precision measurement is attainable for  $\mu_{\tau\tau}^{ZS} > 0.96$ .
- **$bb$  channel:** A  $5\sigma$  discovery can be achieved for  $\mu_{bb}^{ZS} > 4.2 \times 10^{-3}$ , and a 1% precision measurement for  $\mu_{bb}^{ZS} > 0.13$ .

These results demonstrate that particle-level transformer networks can significantly enhance the sensitivity to light Higgs states and improve the achievable precision of cross-section measurements at future lepton colliders. They provide a concrete example of how machine-learning-assisted analyses can advance the precision Higgs program and probe extended Higgs sectors beyond the Standard Model.

*Applicability to other lepton colliders.* — Although this study is performed using the CEPC baseline detector and luminosity assumptions, the conclusions are broadly applicable to other future  $e^+e^-$  Higgs factories such as FCC-ee [22, 23] and ILC [24–26]. The FCC-ee operates at a similar center-of-mass energy ( $\sqrt{s} = 240\text{--}250$  GeV) with comparable detector performance and slightly lower integrated luminosity, implying that our results can be directly extrapolated with minor scaling in significance ( $Z \propto \sqrt{L}$ ). For the ILC, whose initial Higgs-factory stage runs at 250 GeV with about  $2\text{ ab}^{-1}$  of data and stronger magnetic fields (3.5–5 T), the overall reconstruction efficiencies and resolutions are expected to be similar to those of the CEPC ILD-like detector. Therefore, the machine-learning improvements demonstrated here remain valid, though the attainable precision scales with the available statistics. Future dedicated studies including detector-specific simulations for FCC-ee and ILC would further quantify these effects.

## ACKNOWLEDGMENTS

This work was supported by the National Natural Science Foundation of China under Grant No. 12275066 and by the startup research funds of Henan University. The work of K. Wang is also supported by the Open Project of the Shanghai Key Laboratory of Particle Physics and Cosmology under Grant No. 22DZ2229013-3.

---

- [1] S. Chatrchyan *et al.* (CMS), *Phys. Lett. B* **716**, 30 (2012), arXiv:1207.7235 [hep-ex].
- [2] G. Aad *et al.* (ATLAS), *Phys. Lett. B* **716**, 1 (2012), arXiv:1207.7214 [hep-ex].
- [3] K. Kajantie, M. Laine, K. Rummukainen, and M. E. Shaposhnikov, *Nucl. Phys. B* **466**, 189 (1996), arXiv:hep-lat/9510020.
- [4] G. R. Farrar and M. E. Shaposhnikov, *Phys. Rev. Lett.* **70**, 2833 (1993), [Erratum: *Phys. Rev. Lett.* 71, 210 (1993)], arXiv:hep-ph/9305274.
- [5] M. B. Gavela, P. Hernandez, J. Orloff, and O. Pene, *Mod. Phys. Lett. A* **9**, 795 (1994), arXiv:hep-ph/9312215.
- [6] A. D. Sakharov, *Pisma Zh. Eksp. Teor. Fiz.* **5**, 32 (1967).
- [7] P. Huet and E. Sather, *Phys. Rev. D* **51**, 379 (1995), arXiv:hep-ph/9404302.
- [8] K. Rummukainen, K. Kajantie, M. Laine, M. E. Shaposhnikov, and M. Tsypin, in *5th International Workshop on Thermal Field Theories and Their Applications* (1998) arXiv:hep-ph/9809435.
- [9] Anisha, L. Biermann, C. Englert, and M. Mühlleitner, *JHEP* **08**, 091 (2022), arXiv:2204.06966 [hep-ph].
- [10] R. Barate *et al.* (LEP Working Group for Higgs boson searches, ALEPH, DELPHI, L3, OPAL), *Phys. Lett. B* **565**, 61 (2003), arXiv:hep-ex/0306033.
- [11] A. M. Sirunyan *et al.* (CMS), *Phys. Lett. B* **793**, 320 (2019), arXiv:1811.08459 [hep-ex].
- [12] A. Tumasyan *et al.* (CMS), *JHEP* **07**, 073 (2023), arXiv:2208.02717 [hep-ex].
- [13] A. Hayrapetyan *et al.* (CMS), *Phys. Lett. B* **860**, 139067 (2025), arXiv:2405.18149 [hep-ex].
- [14] (2023).
- [15] P. Sharma, A.-T. Mulaudzi, K. Mosala, T. Mathaha, M. Kumar, B. Mellado, A. Crivellin, M. Titov, M. Ruan, and Y. Fang, *Phys. Lett. B* **870**, 139953 (2025), arXiv:2407.16806 [hep-ph].

ph].

- [16] K. Wang and J. Zhu, *Chin. Phys. C* **48**, 073105 (2024), arXiv:2402.11232 [hep-ph].
- [17] J. Dutta, J. Lahiri, C. Li, G. Moortgat-Pick, S. F. Tabira, and J. A. Ziegler, *Eur. Phys. J. C* **84**, 926 (2024), arXiv:2308.05653 [hep-ph].
- [18] Y. Dong, K. Wang, and J. Zhu, *Phys. Rev. D* **112**, 055013 (2025), arXiv:2410.13636 [hep-ph].
- [19] H. Xu, Y. Wang, X.-F. Han, and L. Wang, (2025), arXiv:2505.03592 [hep-ph].
- [20] G. L. Bayatian *et al.* (CMS), *J. Phys. G* **34**, 995 (2007).
- [21] M. Capeans, G. Darbo, K. Einsweiler, M. Elsing, T. Flick, M. Garcia-Sciveres, C. Gemme, H. Pernegger, O. Rohne, and R. Vuillermet (ATLAS), (2010).
- [22] A. Abada *et al.* (FCC), *Eur. Phys. J. ST* **228**, 261 (2019).
- [23] A. Abada *et al.* (FCC), *Eur. Phys. J. C* **79**, 474 (2019).
- [24] (2013), arXiv:1306.6352 [hep-ph].
- [25] (2013), arXiv:1306.6327 [physics.acc-ph].
- [26] D. M. Asner *et al.*, in *Snowmass 2013: Snowmass on the Mississippi* (2013) arXiv:1310.0763 [hep-ph].
- [27] M. Dong *et al.* (CEPC Study Group), (2018), arXiv:1811.10545 [hep-ex].
- [28] (2018), arXiv:1809.00285 [physics.acc-ph].
- [29] F. An *et al.*, *Chin. Phys. C* **43**, 043002 (2019), arXiv:1810.09037 [hep-ex].
- [30] W. Abdallah *et al.* (CEPC Study Group), *Radiat. Detect. Technol. Methods* **8**, 1 (2024), [Erratum: Radiat.Detect.Technol.Methods 9, 184–192 (2025)], arXiv:2312.14363 [physics.acc-ph].
- [31] P. T. Komiske, E. M. Metodiev, and J. Thaler, *JHEP* **01**, 121 (2019), arXiv:1810.05165 [hep-ph].
- [32] H. Qu and L. Gouskos, *Phys. Rev. D* **101**, 056019 (2020), arXiv:1902.08570 [hep-ph].
- [33] V. Mikuni and F. Canelli, *Eur. Phys. J. Plus* **135**, 463 (2020), arXiv:2001.05311 [physics.data-an].
- [34] V. Mikuni and F. Canelli, *Mach. Learn. Sci. Tech.* **2**, 035027 (2021), arXiv:2102.05073 [physics.data-an].
- [35] S. Gong, Q. Meng, J. Zhang, H. Qu, C. Li, S. Qian, W. Du, Z.-M. Ma, and T.-Y. Liu, *JHEP* **07**, 030 (2022), arXiv:2201.08187 [hep-ph].
- [36] H. Qu, C. Li, and S. Qian, (2022), arXiv:2202.03772 [hep-ph].

[37] Y. Wu, K. Wang, C. Li, H. Qu, and J. Zhu, *Chin. Phys. C* **49**, 013110 (2025), arXiv:2407.08682 [hep-ph].

[38] A. Vaswani, N. Shazeer, N. Parmar, J. Uszkoreit, L. Jones, A. N. Gomez, L. Kaiser, and I. Polosukhin, in *31st International Conference on Neural Information Processing Systems* (2017) arXiv:1706.03762 [cs.CL].

[39] J. Cao, X. Guo, Y. He, P. Wu, and Y. Zhang, *Phys. Rev. D* **95**, 116001 (2017), arXiv:1612.08522 [hep-ph].

[40] K. Wang, F. Wang, J. Zhu, and Q. Jie, *Chin. Phys. C* **42**, 103109 (2018), arXiv:1811.04435 [hep-ph].

[41] W. G. Hollik, C. Li, G. Moortgat-Pick, and S. Paasch, *Eur. Phys. J. C* **81**, 141 (2021), arXiv:2004.14852 [hep-ph].

[42] A. M. Coutinho, A. Karan, V. Miralles, and A. Pich, *JHEP* **02**, 057 (2025), arXiv:2412.14906 [hep-ph].

[43] W. Li, H. Qiao, and J. Zhu, *Chin. Phys. C* **47**, 123102 (2023), arXiv:2212.11739 [hep-ph].

[44] F. Domingo, U. Ellwanger, and C. Hugonie, *Eur. Phys. J. C* **82**, 1074 (2022), arXiv:2209.03863 [hep-ph].

[45] J. Cao, X. Jia, J. Lian, and L. Meng, *Phys. Rev. D* **109**, 075001 (2024), arXiv:2310.08436 [hep-ph].

[46] W. Li, H. Qiao, K. Wang, and J. Zhu, (2023), arXiv:2312.17599 [hep-ph].

[47] J. Lian, *Phys. Rev. D* **110**, 115018 (2024), arXiv:2406.10969 [hep-ph].

[48] J. Cao, X. Jia, and J. Lian, *Phys. Rev. D* **110**, 115039 (2024), arXiv:2402.15847 [hep-ph].

[49] U. Ellwanger and C. Hugonie, *Eur. Phys. J. C* **83**, 1138 (2023), arXiv:2309.07838 [hep-ph].

[50] U. Ellwanger, C. Hugonie, S. F. King, and S. Moretti, *Eur. Phys. J. C* **84**, 788 (2024), arXiv:2404.19338 [hep-ph].

[51] T. Biekötter and M. O. Olea-Romacho, *JHEP* **10**, 215 (2021), arXiv:2108.10864 [hep-ph].

[52] T. Biekötter, S. Heinemeyer, and G. Weiglein, *Phys. Lett. B* **846**, 138217 (2023), arXiv:2303.12018 [hep-ph].

[53] G. Arcadi, G. Busoni, D. Cabo-Almeida, and N. Krishnan, *Phys. Rev. D* **110**, 115028 (2024), arXiv:2311.14486 [hep-ph].

[54] A. Khanna, S. Moretti, and A. Sarkar, (2024), arXiv:2409.02587 [hep-ph].

[55] R. Benbrik, M. Boukidi, and S. Moretti, *Phys. Rev. D* **110**, 115030 (2024), arXiv:2405.02899 [hep-ph].

[56] A. Khanna, S. Moretti, and A. Sarkar, (2025), arXiv:2509.06017 [hep-ph].

[57] A. Belyaev, R. Benbrik, M. Boukidi, M. Chakraborti, S. Moretti, and S. Semlali, *JHEP* **05**, 209 (2024), arXiv:2306.09029 [hep-ph].

[58] S. Ashanujjaman, S. Banik, G. Coloretti, A. Crivellin, B. Mellado, and A.-T. Mulaudzi, *Phys. Rev. D* **108**, L091704 (2023), arXiv:2306.15722 [hep-ph].

[59] Z.-f. Ge, F.-Y. Niu, and J.-L. Yang, *Eur. Phys. J. C* **84**, 548 (2024), arXiv:2405.07243 [hep-ph].

[60] A. Ahriche, M. L. Bellile, M. O. Khojali, M. Kumar, and A.-T. Mulaudzi, *Phys. Rev. D* **110**, 015025 (2024), arXiv:2311.08297 [hep-ph].

[61] P. S. B. Dev, R. N. Mohapatra, and Y. Zhang, *Phys. Lett. B* **849**, 138481 (2024), arXiv:2312.17733 [hep-ph].

[62] Q. Chang, X. Du, and P. Zhu, (2025), arXiv:2509.26155 [hep-ph].

[63] R. Benbrik, M. Boukidi, K. Kahime, S. Moretti, L. Rahili, and B. Taki, *Phys. Lett. B* **868**, 139688 (2025), arXiv:2505.07811 [hep-ph].

[64] S. Yaser Ayazi, M. Hosseini, S. Pakhtinat Mehdiabadi, and R. Rouzbehi, *Phys. Rev. D* **110**, 055004 (2024), arXiv:2405.01132 [hep-ph].

[65] L. Liu, H. Qiao, K. Wang, and J. Zhu, *Chin. Phys. C* **43**, 023104 (2019), arXiv:1812.00107 [hep-ph].

[66] S. Banik, A. Crivellin, S. Iguro, and T. Kitahara, *Phys. Rev. D* **108**, 075011 (2023), arXiv:2303.11351 [hep-ph].

[67] S. Heinemeyer, C. Li, F. Lika, G. Moortgat-Pick, and S. Paasch, *Phys. Rev. D* **106**, 075003 (2022), arXiv:2112.11958 [hep-ph].

[68] T. Biekötter, M. Chakraborti, and S. Heinemeyer, *Eur. Phys. J. C* **80**, 2 (2020), arXiv:1903.11661 [hep-ph].

[69] T. Biekötter, A. Grohsjean, S. Heinemeyer, C. Schwanenberger, and G. Weiglein, *Eur. Phys. J. C* **82**, 178 (2022), arXiv:2109.01128 [hep-ph].

[70] J. A. Aguilar-Saavedra, H. B. Câmara, F. R. Joaquim, and J. F. Seabra, *Phys. Rev. D* **108**, 075020 (2023), arXiv:2307.03768 [hep-ph].

[71] T. Biekötter, S. Heinemeyer, and G. Weiglein, *JHEP* **08**, 201 (2022), arXiv:2203.13180 [hep-ph].

[72] M. Y. Sassi and G. Moortgat-Pick, (2025), arXiv:2506.14880 [hep-ph].

[73] C.-Y. Chen, M. Freid, and M. Sher, *Phys. Rev. D* **89**, 075009 (2014), arXiv:1312.3949 [hep-ph].

[74] A. Drozd, B. Grzadkowski, J. F. Gunion, and Y. Jiang, *JHEP* **11**, 105 (2014), arXiv:1408.2106 [hep-ph].

[75] M. Mühlleitner, M. O. P. Sampaio, R. Santos, and J. Wittbrodt, *JHEP* **03**, 094 (2017), arXiv:1612.01309 [hep-ph].

[76] R. Coimbra, M. O. P. Sampaio, and R. Santos, *Eur. Phys. J. C* **73**, 2428 (2013), arXiv:1301.2599 [hep-ph].

[77] M. Mühlleitner, M. O. P. Sampaio, R. Santos, and J. Wittbrodt, *Eur. Phys. J. C* **82**, 198 (2022), arXiv:2007.02985 [hep-ph].

[78] S. Kanemura, T. Kubota, and E. Takasugi, *Phys. Lett. B* **313**, 155 (1993), arXiv:hep-ph/9303263.

[79] W. G. Hollik, G. Weiglein, and J. Wittbrodt, *JHEP* **03**, 109 (2019), arXiv:1812.04644 [hep-ph].

[80] P. M. Ferreira, M. Mühlleitner, R. Santos, G. Weiglein, and J. Wittbrodt, *JHEP* **09**, 006 (2019), arXiv:1905.10234 [hep-ph].

[81] J. Haller, A. Hoecker, R. Kogler, K. Mönig, T. Peiffer, and J. Stelzer, *Eur. Phys. J. C* **78**, 675 (2018), arXiv:1803.01853 [hep-ph].

[82] P. Bechtle, D. Dercks, S. Heinemeyer, T. Klingl, T. Stefaniak, G. Weiglein, and J. Wittbrodt, *Eur. Phys. J. C* **80**, 1211 (2020), arXiv:2006.06007 [hep-ph].

[83] P. Bechtle, S. Heinemeyer, T. Klingl, T. Stefaniak, G. Weiglein, and J. Wittbrodt, *Eur. Phys. J. C* **81**, 145 (2021), arXiv:2012.09197 [hep-ph].

[84] G. Aad *et al.* (ATLAS), *JHEP* **01**, 053 (2025), arXiv:2407.07546 [hep-ex].

[85] I. Engeln, M. Mühlleitner, and J. Wittbrodt, *Comput. Phys. Commun.* **234**, 256 (2019), arXiv:1805.00966 [hep-ph].

[86] S. Navas *et al.* (Particle Data Group), *Phys. Rev. D* **110**, 030001 (2024).

[87] Z. Chen, Y. Yang, M. Ruan, D. Wang, G. Li, S. Jin, and Y. Ban, *Chin. Phys. C* **41**, 023003 (2017), arXiv:1601.05352 [hep-ex].

[88] J. Alwall, M. Herquet, F. Maltoni, O. Mattelaer, and T. Stelzer, *JHEP* **06**, 128 (2011), arXiv:1106.0522 [hep-ph].

[89] J. Alwall, R. Frederix, S. Frixione, V. Hirschi, F. Maltoni, O. Mattelaer, H. S. Shao, T. Stelzer, P. Torrielli, and M. Zaro, *JHEP* **07**, 079 (2014), arXiv:1405.0301 [hep-ph].

[90] M. Cacciari, G. P. Salam, and G. Soyez, *JHEP* **04**, 063 (2008), arXiv:0802.1189 [hep-ph].

[91] D. Yu, M. Ruan, V. Boudry, H. Videau, J.-C. Brient, Z. Wu, Q. Ouyang, Y. Xu, and X. Chen, *Eur. Phys. J. C* **80**, 7 (2020).

[92] T. Sjöstrand, S. Ask, J. R. Christiansen, R. Corke, N. Desai, P. Ilten, S. Mrenna, S. Prestel, C. O. Rasmussen, and P. Z. Skands, *Comput. Phys. Commun.* **191**, 159 (2015), arXiv:1410.3012 [hep-ph].

[93] J. de Favereau, C. Delaere, P. Demin, A. Giannanco, V. Lemaître, A. Mertens, and M. Selvaggi (DELPHES 3), *JHEP* **02**, 057 (2014), arXiv:1307.6346 [hep-ex].

[94] M. Selvaggi, *J. Phys. Conf. Ser.* **523**, 012033 (2014).

[95] Y. Zhu, H. Liang, Y. Wang, Y. Che, H. Wang, C. Zhou, H. Qu, and M. Ruan, (2025), arXiv:2506.11783 [hep-ex].

[96] G. Cowan, K. Cranmer, E. Gross, and O. Vitells, *Eur. Phys. J. C* **71**, 1554 (2011), [Erratum: Eur.Phys.J.C 73, 2501 (2013)], arXiv:1007.1727 [physics.data-an].